UNIVERSITY OF BIRMINGHAM

University of Birmingham
Research at Birmingham

Microwave dielectric sensing of free-flowing, single, living cells in aqueous suspension

Watts, Clare; Hanham, Stephen; Armstrong, James; Ahmad, Munir; Stevens, Molly; Klein, Norbert

Document Version
Peer reviewed version

[Link to publication on Research at Birmingham portal](#)

Microwave Dielectric Sensing of Free-Flowing, Single, Living Cells in Aqueous Suspension

C. Watts, S. M. Hanham, *Member, IEEE*, J. P. K. Armstrong,
M. M. Ahmad, M. M. Stevens, and N. Klein

MICROFLUIDICS MINIMISE INTERACTION VOLUME FOR SINGLE CELL SENSITIVITY

SPLIT RING FOCUSSES ELECTRIC FIELD STRENGTH

COUPLED RESONATORS ALLOW DISPOSABLE CHIPS AND HIGH Q

HIGH FREQUENCY PENETRATES CELL MEMBRANE

A coupled resonator system for microwave dielectric measurements of single, viable, free-flowing cells is presented.

Take-Home Messages
- An inductively-coupled resonator assembly is shown to allow the detection of significantly sub-wavelength diameter biological cells by combining the strong field confinement provided by a split ring resonator with the high quality factor resonance of a dielectric resonator.
- Measurements of single, free-flowing cells in a natural aqueous environment at ~10 GHz have been carried out using a coupled resonator sensor, without the need for trapping, immobilizing, culturing or fixing cells in high-field areas.
- The coupled resonator approach proposed in this work shows potential as a method of discrimination of cells based on hydration levels, which in other works has been linked to carcinogenesis, as well as cancer aggressiveness grade; therefore the sensor described herein may represent an alternative method of cancer diagnosis or disease progression monitoring *via* non-invasive liquid biopsies.
- In this paper, measurements of living, free-flowing, single cells in aqueous buffer solution, at a frequency sensitive to cell water content, have been made.
- The inductive coupling employed in this sensor allows for physical separation of the sensing elements from microwave electronics, allowing for cheap, disposable chips to be used with biological fluids.

Microwave Dielectric Sensing of Free-Flowing, Single, Living Cells in Aqueous Suspension

C. Watts, S. M. Hanham, Member, IEEE, J. P. K. Armstrong,
M. M. Ahmad, M. M. Stevens, and N. Klein

Abstract: Dielectric measurements offer the possibility of highly sensitive detection of physical cell properties, and are of interest for clinical applications due to their non-destructive nature and the lack of need for cell labelling. Here we report sensitive measurements on single, living, free-flowing cells (not electrostatically or dielectrophoretically trapped, cultured or fixed directly on sensing elements) in aqueous medium at ~9.8 GHz taken using a coupled dielectric-split ring resonator assembly. Inductive coupling between the two resonators enabled separation of microfluidic chips from RF connectors and allowed for time-resolved continuous-wave measurements on flowing single cells *via* the coaxial ports of a dielectric-loaded microwave cavity. Analysis *via* an equivalent circuit model showed that the novel resonator assembly maintained the permittivity-dependent sensitivity of a split ring resonator while operating at quality factors >1000 with lossy aqueous media (typically ~1900). Using a microfluidic channel with a 300×300 µm cross section, at a water-loaded resonant amplitude of ~-22 dB at 0 dBm input power level, shifts in amplitude due to individual cells passing through the sensing region of up to -0.0015 dB were observed. Correlations between averaged amplitude shifts and cell size as well as material properties demonstrate the diagnostic potential of this technique.

Keywords —Biological cells, biosensors, dielectric, microfluidics, microwave sensors, permittivity, resonators.

I. INTRODUCTION

THE innate heterogeneity of cell populations can make measurements of the bulk properties of cells, tumors or tissues difficult to interpret. The ability to individually analyze cells using technologies such as the gold standard fluorescence activated cell sorting (FACS) allows for accurate diagnosis, monitoring of disease progression and downstream separation and study of particular cell types.

The differences in dielectric properties of healthy and malignant cells and tissues have been explored since the 1920s [1], and advances in understanding and manufacturing have led to the development of microwave frequency technologies for skin cancer detection [2] and imaging of breast and liver cancer [3]. At frequencies from DC to ~2 GHz, the interaction between electric fields and cells is dominated by cell membrane effects, known in the literature as α and β relaxations [4]–[6]. Approaches that use these cell membrane-sensitive frequencies show high sensitivity to single cells and are able to differentiate clinically significant sub-populations. The differences in cell membrane morphology have been used to distinguish between white blood cell populations [7] as well as between normal and malignant cell populations, due to increased cell surface area and roughness [8]. At these frequencies, analysis technologies operating on the single-cell level range from the ubiquitous Coulter counter, used since the 1950s as a standard cell enumeration technique [9], to ApoStream®, a cutting-edge technology currently in development, which is capable of both differentiating and separating circulating tumor cells (CTCs) from other circulating blood cells using the inherent differences between normal and healthy membranes [10], [11]. At frequencies above ~2 GHz the effects from cell membranes start to become insignificant, and up to around 40 GHz the interaction is dominated by the dielectric relaxation of water molecules. This allows the electric fields to penetrate the cells and interact with intercellular water molecules. Therefore, in theory, this

C. Watts and N. Klein are with the Department of Materials and the Centre for Terahertz Science and Engineering, Imperial College London, SW7 2AZ, London, UK (email: c.watts13@imperial.ac.uk; n.klein@imperial.ac.uk). All correspondence should be addressed to N. Klein.

S. M. Hanham was with Imperial College London. He is now with the Department of Electronic, Electrical and Systems Engineering, University of Birmingham, B15 2TT, Birmingham, UK (email: stephen.hanham@ieee.org).

J. P. K. Armstrong and M. M. Stevens are with the Department of Bioengineering and Institute for Biomedical Engineering, Department of Materials, Imperial College London (email: james.armstrong@imperial.ac.uk; m.stevens@imperial.ac.uk).

M. M. Ahmad is with the Department of Electrical and Electronic Engineering and the Centre for Terahertz Science and Engineering, Imperial College London (email: m.m.ahmad@imperial.ac.uk).

Raw data is available on request from rdm-enquiries@imperial.ac.uk.

frequency regime allows a non-contact, non-destructive and label-free method to analyze the relative water content of cells. Given that cell hydration has been linked to carcinogenesis [12], and water content of tissues is routinely used in MRI to define the extent of tumors [13], this method could lead to a low cost cancer detection technique requiring non-invasive liquid biopsies. Indeed, wideband investigations on cell cultures show that between 10 and 20 GHz the dominant response is that of the reorientation of water molecules, with differences seen between normal and malignant cells [14]. In addition, these frequencies are less adversely affected by losses due to physiological ionic concentrations, allowing for detection in biological medium [15].

Many different approaches have been used to reduce the interaction between the aqueous suspending medium and the electric field in order to increase sensitivity. For instance by using highly concentrated cell suspensions, as in a recent report demonstrating lymphoma cell sub-populations discrimination using broadband characterization [16]. Using a similar CPW approach, suspensions of both live and dead *E. coli* have been characterized over a broad frequency range (0.5-20 GHz), with sensitivity down to ~15 individual bacteria [17]. For single cell approaches, attempts have been made to reduce dielectric losses from water by isolating the sensing elements from the liquid, however, this negatively affects the achievable sensitivity [18]. Electrostatically trapping cells directly in high field regions has been successfully used [19], while hydrodynamic trapping of single cells has allowed broadband characterization up to 40 GHz [20], though these are not high-throughput approaches. Culturing or otherwise adhering cells directly on top of capacitive sensing elements, often followed by drying or chemical fixation in order to avoid aqueous dielectric losses, has shown very high sensitivity down to single cell resolution [18], [21]–[23] and has given clinically relevant information, such as the aggressiveness grade of different cancerous cell populations [24], [25]. However, these approaches are batch processes that do not have high throughput potential, and many methods destroy the cell sample, which hinders down-stream investigation. Even higher frequency approaches, with greater field confinement and lower losses from water, have been proposed for single-cell sensing [26], [27], though at these frequencies the contrast in permittivity between water and the constituents of cells is low. Dielectric resonator (DR) based approaches have also been explored for high quality (Q) factor narrowband measurements, and while whispering-gallery modes allow for accurate dielectric measurements on nanoliter volumes of liquids [28]–[30], this approach provides insufficient spatial confinement to detect single cells passing through a microfluidic channel. Split ring resonators (SRRs) at 2-3 GHz have been used to detect [31] and even measure the dielectric properties of single, flowing polystyrene spheres [18]. Moreover, at frequencies above 2 GHz, single stationary or flowing polystyrene microspheres can be detected [18], [32]. Coupled dielectric-planar SRR

resonator devices have been shown to increase the Q factor of the SRR sensing element by ~40 fold [33]. However, unlike biological cells, polystyrene presents a large permittivity contrast to the surrounding water. A split ring resonator operating at 2.5 GHz has also shown sensitivity to suspensions of *E. coli* in medium at 2.5 GHz, showing a linear response to concentration down to ~6 × 10^6 cells/mL, and Q factors of <100 [34].

High frequency approaches to single cell sensing is an active area of research, and significant progress has been made recently. An approach utilizing capacitance measurements at multiple high frequencies (6.5-30 GHz) has shown ability to differentiate between normal and malignant cell lines in aqueous media in a high-throughput device, employing flow focusing to control cell position [35]. At lower frequencies a simple interferometric device has shown some sensitivity to malignant and normal breast cell lines [36], while planar split ring structures have been used to detect and differentiate giant unilamellar vesicles (>25 μm diameter) at 2.7 and 7.9 GHz [37].

This work introduces a novel, alternative approach based on coupled electromagnetic resonators. The sensor uses cheap, disposable microfluidic chips and is capable of detecting dielectric differences between single cells that are freely flowing in aqueous media, without immobilization, flow focusing, fixing, drying or culturing directly on sensing elements. The sensor combines the sensitivity and spatial confinement of electric fields associated with SRRs, with the temperature stability and high Q factor of dielectric resonator approaches. In addition, the operation of the device is analyzed through an equivalent circuit model, which shows sensitivity unique to the mode of inter-resonator coupling, and shows that higher sensitivities are still achievable. These features make this technology a promising approach for clinically relevant measurements on single cells.

II. RESULTS AND DISCUSSION

A. Sensor description

Following simulations, a sensor was designed comprising two inductively coupled microwave resonators: a cylindrical dielectric resonator (DR) made from a BaZnTa ceramic with a dielectric permittivity of 29 and high Q factors of *ca.* 10,000 at 10 GHz; and a gold thin-film double split ring resonator (DSRR) deposited on a 130 μm thick glass coverslip. Standard microfabrication techniques were used to fabricate the DSRR. 130 μm thick 22 × 64 mm borosilicate glass coverslips were sputter coated with a thin (100-200 nm) adhesion layer of chromium followed by electroplating of a thicker (2 μm) gold layer. Substrates are then spin coated with S1813 and photolithography is used to selectively remove metal *via* wet etching to produce split ring structures. The DR was arranged inside a cylindrical copper cavity (height 7 mm, diameter 18 mm) directly underneath an aperture in the cavity lid. The glass coverslip was placed on top of the lid so that the DSRR faced upwards and was aligned coaxially above the DR in the centre of the aperture,
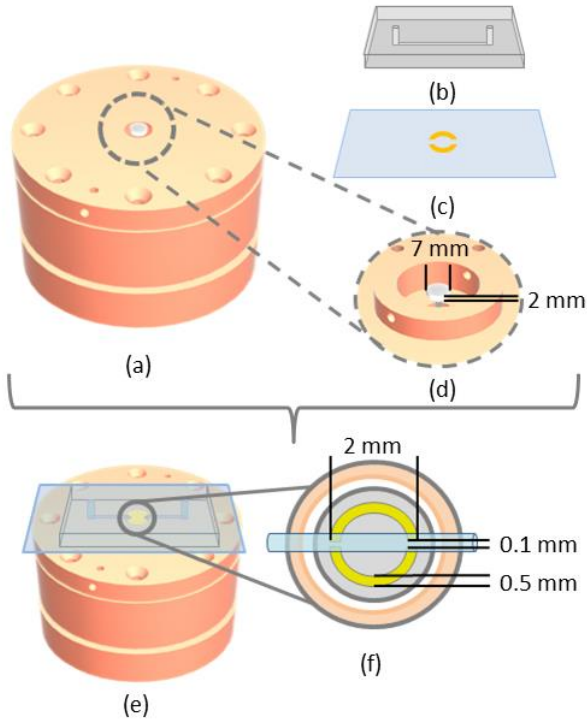
Fig. 1. Schematics of the sensor. (a) Copper housing of the dielectric resonator (DR), showing the cavity, base, lid and holes for coupling loops. (b) The molded PDMS microfluidic channel, shown open (unsealed). (c) The gold thin film double split ring resonator (DSRR) evaporated onto a borosilicate glass coverslip substrate. (d) The DR in the copper cavity, without the lid to show the dimensions. (e) The fully assembled system showing the copper housing, both resonators, and the microfluidic chip assembly on top of the aperture. (f) The alignment of the DR (grey circle), aperture (white circle), DSRR (gold split ring) and microfluidic channel (blue), showing the dimensions of the DSRR.

as shown in Fig. 1.

The fundamental $TE_{01\delta}$ electromagnetic mode of the dielectric resonator at $f_{DR} = 9.81$ GHz was excited *via* two coaxial coupling loops configured for transmission measurements.

The DSRR was inductively coupled with the DR *via* the aperture in the lid of the cavity, as shown in Fig. 2 (a). A linear microfluidic channel (2-3 cm long, ~300 μm wide and tall) cast in polydimethylsiloxane (PDMS) was sealed over the DSRR, so that the glass coverslip of the DSRR formed the base of the channel. The channel was manually aligned so that it passed over the two gaps in the DSRR, with a small area of metal protruding into the channel, as shown in Fig. 1 (f). This set-up enabled liquid pumped through the channel to be directly exposed to the electric field of the DSSR. Fig. 3 shows the measured resonance frequency and Q factor of the device under different conditions, demonstrating that the sensor maintains high water-loaded Q factors. The Q factor of the DR in the copper cavity (Q_{DR}) was <7000, limited by the dielectric losses of the ceramic and Ohmic losses in the walls of the cavity and around the aperture. Placing the glass coverslip with DSRR over the aperture caused a slight decrease in resonant frequency due to the permittivity of the

glass, but did not result in a significant reduction of the Q factor ($Q_{DR+DSRR}$) due to the weak nature of the coupling between the $TE_{01\delta}$ mode of the DR and the fundamental mode of the DSRR. The PDMS channel further increased the dielectric load on the DR and decreased both the resonance frequency and the Q factor ($Q_{channel}$). When the channel was filled with water, the change in Q factor (Q_{water}) was significant. This was due to an increase in coupling strength between the DR and DSRR caused by the permittivity of the
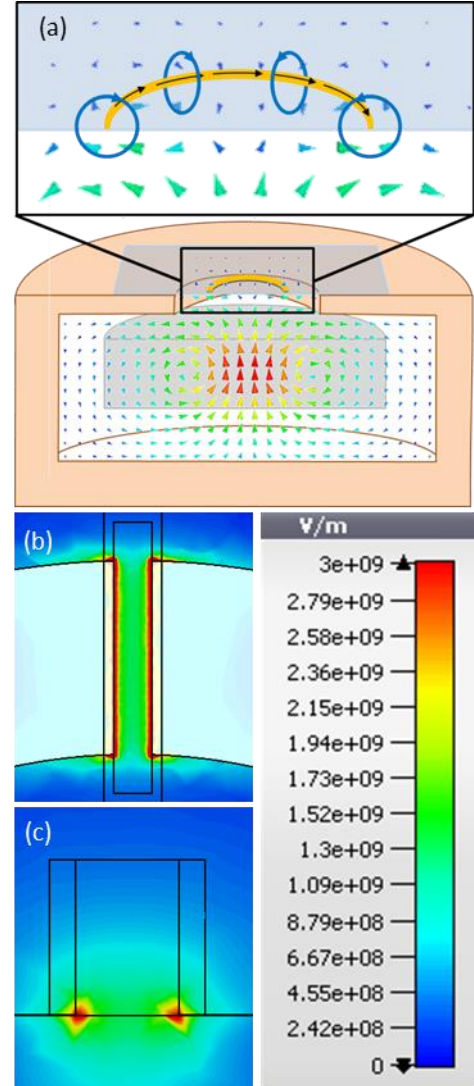
Fig. 2. Schematic of the electromagnetic field distribution in the coupled resonator system. (a) is a cross section of the coupled-resonator assembly showing a snapshot of the magnetic field in and around the DR in the cavity, as well as the protrusion of the magnetic field through the aperture and its interaction with the ring, which is expanded in the box and includes the induced currents in the metal (black arrows) and the resulting magnetic field (blue arrowed circles) wrapping around one half of the DSRR, opposing the magnetic field of the DR. (b) and (c) are heat maps of the electric field distribution in the vicinity of the DSRR gap from CST Microwave Studio simulations, with (b) showing the field strength (red denoting the strongest field and blue the lowest) from above the gap, and (c) as a cross section of the channel in the middle of the gap. Black outlines denote the walls of the channel (outer) and the edges of the metal (inner). For both (b) and (c), the channel is filled with air ($\varepsilon' = 1$, $tan\delta = 0$). A color scale bar for the electric field strength, in V/m is shown on the right. For the eigenmode solver used, the total stored electromagnetic field energy is 1J.

water decreasing the resonance frequency and lowering the Q factor of the DSRR. This had the effect of both increasing the resonant frequency and decreasing the Q factor of the coupled system. The operation of the coupled resonator sensor was illustrated by the measurements of ethanol solutions, which show that a reduction in permittivity of the liquid in the channel led to an increase in inter-resonator coupling and therefore a reduction in Q factor, without significantly changing the resonant frequency. For this reason, for measurements on flowing single particles it was sufficient to measure the magnitude of S₂₁ in continuous wave at the peak frequency, rather than recording the full resonance sweep, which significantly sped up measurements. In the same way, particles with a different permittivity to the surrounding medium passing through these sensing regions caused a change in the capacitance and hence the resonant frequency of the DSRR, which was detected as a change in the transmission properties of the DR. The inter-resonator coupling effect is further elucidated by the equivalent circuit model which is discussed further in the Appendix, along with ethanol solution measurements.

For CW measurements, the resonance frequency of the water loaded DSSR (f_{DSRR}) was designed such that $f_{DSRR} + 1/2 \cdot \Delta f_{1/2,\ DSRR} \approx f_{DR}$ (where $\Delta f_{1/2,\ DSRR}$ is the full width at -3 dB power of the DSRR and f_{DR} is the resonance frequency of the DR) in order to maximize the change in Q factor of the coupled mode when a cell passed through the capacitive gaps. According to an equivalent circuit analysis, which is given in the appendix, the coupled resonator system has the same sensitivity for cell detection

as a single DSSR, but without the need to measure Q factors close to unity. In fact, the measured Q factors of the coupled system with water-loaded channels were of the order of 1,000, and all resonance measurements were taken *via* the coaxial ports of the cavity. Individual cells passing through the channel led to a small decrease in the Q factor of the coupled mode. In turn, this led to a reduction in the forward transmission coefficient of the resonator ($|S_{21}|$) at the resonant frequency by a fraction of a dB.

As elucidated by the equivalent circuit model and discussed in the appendix, changes in the interaction volume between the capacitive electric field and the liquid under test affected the DSRR properties, and was predicted to affect its sensitivity to small changes in the permittivity of the liquid. For this reason, different channels and different alignments between a channel and the DSRR resulted in different overall Q factors and predicted sensitivity. Thus, in order to collect comparative results of different targets, one unchanged assembly was used for all measurements.

B. Real-time measurements

Polystyrene microspheres (11.00 ± 0.25 μm and 24.90 ± 0.77 μm diameter, Polysciences) were suspended in deionized (DI) water at a concentration of ~50,000 -100,000 particles/mL, while C2C12 Myoblasts (ATCC (ATCC® CRL-1772™), Human Mesenchymal Stem Cells (HMSCs, Lonza), and THP-1 Monocytes (ATCC® TIB-202™) were cultured under normal conditions, then re-suspended in phosphate buffered saline (PBS) at a concentration of ~100,000 cells/mL. A Rohde & Schwarz ZVA 24 vector network analyzer (VNA) was used to make transmission
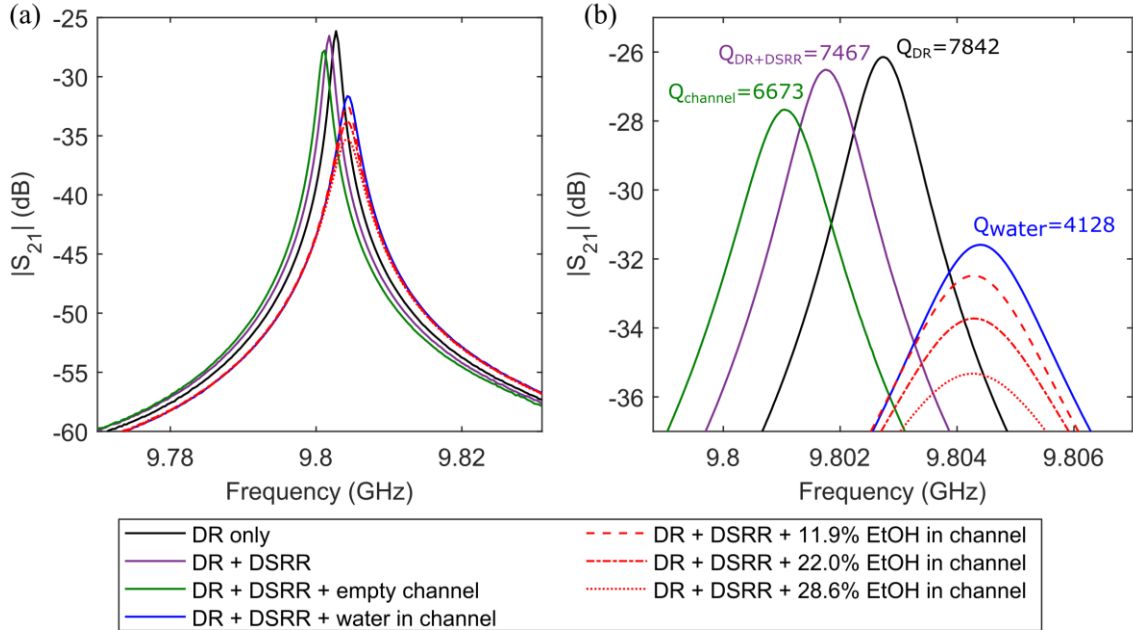
Fig. 3. Plots of measured |S₂₁| of the coupled resonator setup under different conditions. The DR alone (black trace), the DR coupled with the DSRR only (purple trace), the DR coupled with the DSRR with the empty PDMS channel sealed on top (green trace), the DR coupled with the DSRR with a water-filled channel sealed on top (blue trace) and the DR coupled with the DSRR with the channel sealed on top filled with ethanol solutions of various concentrations (red traces). All sweeps shown in (a) were taken over a span of 50 MHz using an IFBW of 1 kHz, an input power of 0 dBm, and 1601 points, while in (b) the peaks are enhanced for clarity, with the calculated quality factors of different conditions shown next to the corresponding peaks in the same colors. In all cases, quality factors are calculated as $f_c/\Delta f_{1/2}$, where f_c is the peak frequency in Hz, and $\Delta f_{1/2}$ is the full width at half power in Hz, and the half power level is determined as the power at -3dB from the peak.

measurements for polystyrene microspheres and cells. All real-time measurements were done by operating the VNA in continuous wave (CW) mode at the coupled-resonator peak frequency (~9.8 GHz) with a power level of 0 dBm and an IFBW of 10 Hz. All experiments were carried out under normal laboratory environment conditions.

CW measurements of $|S_{21}|$ of the coupled resonator at the unperturbed resonance frequency allowed fast, real-time measurements to be taken as targets passed through the gap. By simultaneously triggering $|S_{21}|$ measurement and the high-speed camera to capture an image of the capacitive gap, amplitude shifts could be correlated to targets passing through the sensing region. By continuously monitoring the video feed from the sensing gap, whilst simultaneously manipulating the flow of the cell suspension using a pressure pump, it can be visually determined when a single cell is present in the capacitive gap. Once a single cell is present and can be precisely controlled using the pressure pump, the measurement is started, whereby the video footage and $|S_{21}|$ data are captured simultaneously, while the cell is moved backwards and forwards through the gap. This also allows for checking the results during post-processing in great detail
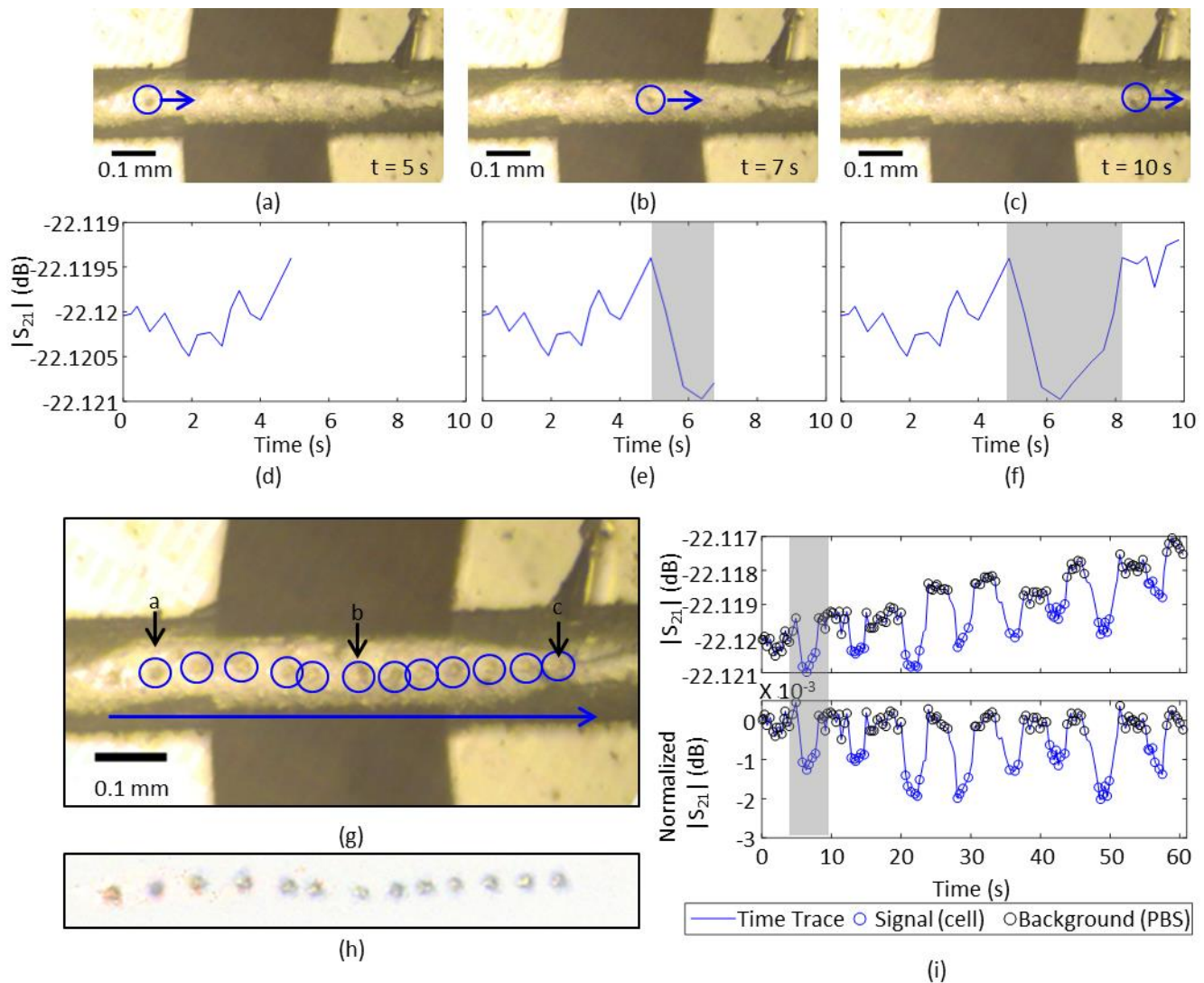

Fig. 4. Repeat measurements of a single C2C12 cell. (a), (b) and (c) are optical microscope images captured by the high speed camera showing a C2C12 cell (highlighted by the blue circle) in the capacitive gap at different times, travelling from left to right through the gap (as indicated by the blue arrows), and moving forward in time from (a) to (c) by 5 s, as indicated in the bottom right of each image. (d), (e) and (f) show the corresponding real-time amplitude data traces for each time point shown in (a), (b) and (c), respectively, with the data taken while the cell is in the capacitive gap highlighted in pale grey. (g) shows a composite image of the cell pass in Fig. 4 (a-c), showing the position of the cell at each measurement point during one pass through the capacitive gap. Images of the gap are taken by a high speed camera approximately every 0.4 seconds. The cell in each frame is circled in blue, while the direction that the cell is travelling in is shown by the large blue arrow. The position of the cell at the measurement points shown in (a) to (c) is indicated with a black arrow and corresponding label (a, b and c). (h) is an overlay of all images taken of the cell during the same pass, showing the images used for cell size determination. The upper plot of (i) shows the raw amplitude data from the sensor (blue line, which is a linear interpolation of the raw $|S_{21}|$ data points) showing a total of 8 consecutive cell passes, as the same cell is moved backwards and forwards through the capacitive gap 8 times. Measurements taken with the cell in the gap are circled in blue, and measurements taken without the cell in the gap are circled in black. The lower plot of (i) shows the same data after background subtraction and normalization around 0 dB. In both plots of (i) the first measured cell pass (highlighted in pale grey) corresponds to the measurements shown in detail in (a) to (h), where the same data points are also highlighted in pale grey in (e) and (f).

and at reduced speed so that any instances of multiple cells in the gap or cell clusters can be removed from the final results.

Measurements of $|S_{21}|$ taken with the target (a polystyrene microsphere or cell) in the capacitive gap were referred to as "signal", while measurements of the suspending liquid (DI water, or PBS) were referred to as "reference". Following data collection, a background removal strategy that preserved the standard deviation of reference measurements (measurements taken over time of PBS only flowing through the channel) was implemented, whereby a smoothed fit to the mean of each group of reference measurements was made, then the fit subtracted from all data points in order to normalize the data around 0 dB. The magnitude of shifts away from the reference measurements was then reported relative to zero, rather than to the preceding or subsequent reference measurements, and the variation of both signal and reference measurements were unchanged. This was used rather than a polynomial fit due to occasional large shifts caused by mechanical drift, vibrations or pressure fluctuations.

The stability of CW measurements at 10 GHz is quoted by the VNA manufacturer as typically 0.001 dB at a power level of 0 dBm and an IFBW of 1 kHz. Given the much lower IFBW used, and the small time between measurements of the suspending medium and the target, it was expected that the stability of these measurements should exceed this value. Indeed, the standard deviation of the reference measurements across the biological cell dataset did not exceed 0.0004 dB. In the absence of a known absolute precision of relative measurements of this type, all average amplitude shift values were quoted to a significance level of no more than their standard deviation.

C. Polystyrene sphere measurements

First, polystyrene microspheres of two different diameters were used to test the sensor. The amplitude shift averaged over 13 different 25 µm diameter PS spheres was -0.013 ± 0.004 dB, while for 6 different 11 µm diameter spheres a shift of -0.0008 ± 0.0005 dB was measured. These results showed that the system was capable of detecting particles far smaller than the sensing region (500 µm across). These experiments also showed that the system was sensitive to changes in the path that targets took through the capacitive gaps, with those passing closer to the metal producing much larger shifts. Insufficient control of the height of the particle in the channel also resulted in a large variation between individual target passes. The results of the polystyrene microsphere measurements are summarized in Table 1. The large ratio between the magnitude of shifts observed for the 25 and 11 µm PS microspheres (*ca.* 10) was in good agreement with the volume ratio within their errors, as expected for a homogeneous electric field across the microsphere diameter.

D. Cell measurements

With the system proving to be capable of detecting small particles, it was next tested with three different biological cell types: murine myoblasts (C2C12 cell line), human mesenchymal stem cells (hMSCs), and human peripheral blood monocytes (THP-1 cell line). Example results obtained using C2C12 myoblasts are shown in Fig. 4, which demonstrated clear amplitude shifts when a cell passed through the capacitive sensing region. The C2C12 myoblasts showed, on average, the largest amplitude shifts, followed by hMSCs and then THP-1 monocytes. The average amplitude shifts for all three cell types are summarized in Table 1 and Fig. 5.

The selected cell types exhibited diameter values in the range of 25-30 µm, according to analysis of the video footage recorded by the optical microscopy and camera set up, and amplitude shifts show a correlation with estimated cell size, with larger cells inducing larger shifts. Amplitude shifts from individual cell measurements also showed the same dependence on size. Theoretically, the system should be sensitive only to the amount of water present in the sensing volume. Therefore, from the perspective of the electric fields, the "non-water" contents of a cell (lipids, proteins, DNA *etc.*) act to displace an equivalent volume of water. In this way, both the relative cellular water content and cell size will have an effect upon the signal measured, *i.e.* a larger cell will displace a larger amount of water than a smaller cell with identical hydration, and therefore produce a larger amplitude shift (since all shifts are measured relative to a reference of aqueous suspending medium). This relationship can be seen in Fig. 5 (a).

However, as can be seen in Fig. 5 (b), the amplitude shifts induced by polystyrene microspheres and cells of similar size were very different, showing that the device was not only sensitive to target size, but also to the composition of the target. Polystyrene microspheres showed much larger amplitude shifts than any of the biological cells. This result can be attributed to the higher permittivity contrast between polystyrene microspheres and water than between biological

TABLE I
AMPLITUDE SHIFTS MEASURED FOR BIOLOGICAL CELLS AND
POLYSTYRENE MICROSPHERES

TARGET	$\Delta A \pm 1\,\sigma$ (dB)
C2C12 myoblasts	-0.0015 ± 0.0006
human mesenchymal stem cells (HMSCs)	-0.0011 ± 0.0007
THP-1 monocytes	-0.0007 ± 0.0006
25 µm polystyrene microspheres	-0.013 ± 0.004
11 µm polystyrene microspheres	-0.0008 ± 0.0005

Values are quoted as mean averages to a significance level dependent on the standard deviation (σ) of the data. Error quoted is one standard deviation.
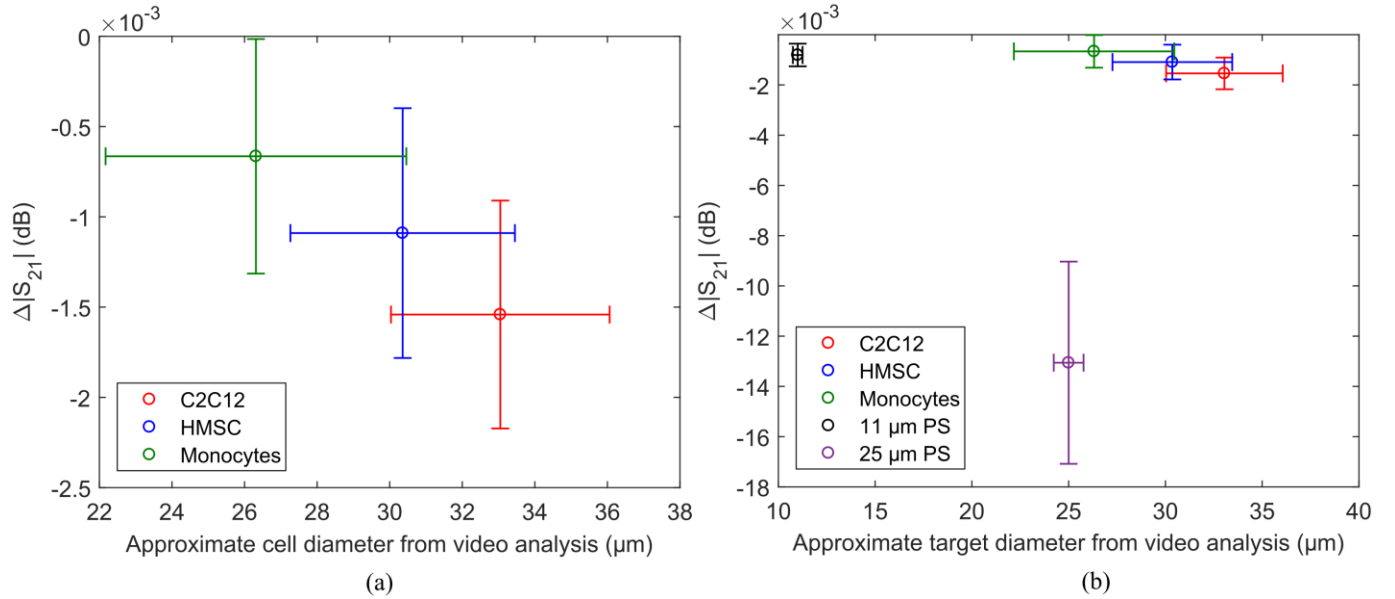
(a)

(b)

Fig. 5. Scatter plots summarising the cell and polystyrene sphere data. (a) shows the average normalised measured amplitude shifts of all three cell types studied and their estimated cell diameters from video analysis, C2C12 cells in red, HMSCs in blue and THP-1 Monocytes in green. Data for the C2C12 cells consists of 754 individual amplitude measurements taken over 5 different cells, while HMSC data consists of 1072 individual amplitude measurements over 7 different cells and monocyte cell data shows 1618 individual amplitude measurements taken over 7 different cells. (b) shows the same data as in (a) alongside 11 and 25 μm diameter polystyrene sphere data. 11 and 25 μm polystyrene microsphere sphere data consists of 386 and 3030 individual amplitude measurements taken over 6 and 13 different spheres, respectively. All error bars denote ±1 standard deviation of the data. All cell diameter estimation was performed using video analysis, while for polystyrene microspheres the diameters and standard deviations are provided by the manufacturer.

cells and water, as polystyrene has a much lower permittivity (2.54 at ~10 GHz [38]) than biological cells, which are highly hydrated and are thus expected to have a permittivity only slightly lower than that of water at ~10 GHz.

III. CONCLUSION

A coupled-resonator sensor operating at ~10 GHz based on a dielectric resonator and thin metal film split ring resonator has been described, which was shown to be capable of measuring individual flowing cells and polystyrene spheres of <30 μm diameter in an aqueous environment.

Through comparison of results from biological cells and similarly sized polystyrene microspheres, we observed that the sensor was responsive to both target size and composition. Therefore, in the case of targets of identical dimensions, the material properties determine the magnitude of the amplitude shift they induce, potentially allowing discrimination between different cell types based on their composition. Low-permittivity polystyrene microspheres resulted in much larger shifts than cells, suggesting that water content is a potential cause for the observed differences. Although it is well known that microwave frequencies are sensitive to water content, for now the variation within the cell measurements is too high to draw reliable conclusions about this dependence for our sensor. Future work will focus on methods to improve the precision of measurements to allow this possible effect to be more fully explored, since the determination of relative water content of flowing, living, cells, in their natural environment, is of obvious clinical significance.

For future applications, integration of a separate method

for cell size determination, for example optical scattering, would allow amplitude shifts to be accurately normalized to cell volume. Ongoing work to optimize the system has already shown that set ups with different channels and rings show even higher sensitivity than reported here (~4 fold increase in amplitude shifts, data not shown). These results indicate that such water-content characterization measurements could be achieved with this system.

APPENDIX

A. Equivalent Circuit Model (ECM)

In order to optimize the coupled resonator system for ultimate sensitivity for cell detection and in order to extract the complex permittivity $\varepsilon^* = \varepsilon' + j\varepsilon''$ of liquids from the measurements we have developed an equivalent circuit model (ECM). Our ECM allows accurate modelling of the measured frequency and quality factor response of the coupled system over a wide range of ε' and ε'' values with two dominant fit parameters.

DSRR. An LC resonant circuit as shown in Fig. 6 (a) is employed to describe the resonance parameters f_{DSRR} and Q_{DSRR} of the DSSR. In Fig. 6 (a), L denotes the induction of each half ring, C_0 the stray capacitance due to the portion of the electric field outside the microfluidic channel, C_d the capacitance owing to the electric field within the liquid filled microfluidic channel and R_d describes the dielectric losses of the liquid inside the microfluidic channel. The resonant parameters of this circuit can be expressed by:

$$\frac{\omega_{DSRR}^2}{\omega_{DSRR,0}^2} = \frac{\varepsilon' - \kappa(\varepsilon')[\varepsilon' - 1]}{\varepsilon'[1 + \kappa(\varepsilon')^2 (tan\delta)^2]} \quad (1)$$

$$\frac{1}{Q_{DSRR}} = \kappa(\varepsilon')tan\delta + \frac{1}{Q_m} \qquad (2)$$

where ω_{DSRR} denotes the resonant frequency for a given filling factor, $\kappa(\varepsilon')$, which describes the fraction of the capacitive electric field energy affected by the liquid sample, while ε' and $tan\delta = \varepsilon''/\varepsilon'$ represent the real permittivity and the loss tangent of the liquid, respectively. $\omega_{DSRR,0}$ represents the resonant frequency of the DSRR for the case of an empty channel. The filling factor is dependent on the real part of the complex permittivity, ε', according to:

$$\kappa(\varepsilon') = \frac{1}{1+\frac{1}{\varepsilon'}\left[\frac{1}{\kappa_0}-1\right]} \qquad (3)$$

with κ_0 denoting the geometric filling factor, which is the effective volume fraction of the capacitor field filled with the liquid. The basic assumption of the ECM is that the electric field distribution in the capacitors is independent of the permittivity of the liquid under test. In order to fit the ECM to experimentally measured resonant parameters of the coupled system, κ_0 is used as a fitting parameter. The quality factor contribution due to Ohmic losses in the DSRR, Q_m, along with $\omega_{DSRR,0}$ are taken from numerical field simulations of the empty DSRR.

Coupled resonators. We next consider an equivalent circuit for the coupled resonator system as shown in Fig. 6 (b). Both resonators, described by their complex impedances, $z_i(\omega)$, with i=1 for the DR and i=2 for the DSRR, are expressed by their generic normalized impedances of a series resonant circuit:

$$z_i(\omega) = \frac{Z(\omega)}{Z_{Li}} = \frac{1}{Q_i} + j\left(\frac{\omega}{\omega_{ri}} - \frac{\omega_{ri}}{\omega}\right) \qquad (4)$$

where z_i is impedance normalized to, Z_{Li}, the line impedance of a transmission line formed by the inductor and capacitor of each resonant circuit and is equal to $\sqrt{L/C_i}$, while Q_i and ω_{ri} denote the quality factor and resonant frequency of the resonators, respectively, with the DR represented with i=1 and the DSRR with i=2.

The resonant parameters of the coupled system are then worked out based on a numerical analysis, over an angular frequency range ω, of the effective impedance at the input port of the circuit shown in Fig. 6 (b) according to:

$$\frac{1}{z_{eff}(\omega)} = \frac{Z_{Li}}{Z_{eff}(\omega)} = \frac{1}{z_1(\omega)\left(1+\frac{\omega^2 k^2}{\omega_{r1}\omega_{r2}z_1(\omega)z_2(\omega)}\right)} \qquad (5)$$

The resonant parameters of the coupled resonances can then be found as they correspond to the frequency and magnitude of the maxima of $\left|\frac{1}{z_{eff}(\omega)}\right|$.

A. Fitting to experimental results

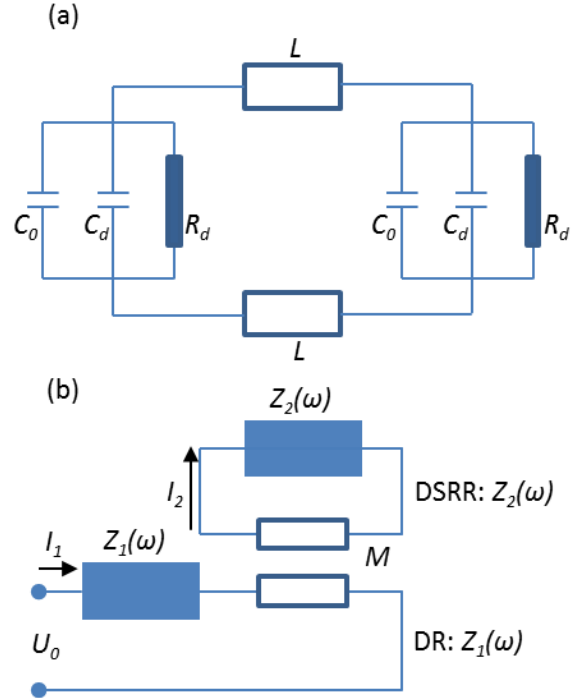In order to ascertain the fitting parameters k, and κ_0,

Fig. 6. Schematic of the equivalent circuit used to approximate the coupled resonator sensor. (a) Equivalent circuit for modelling of the resonance parameters of the DSSR with partially filled capacitors. (b) Equivalent circuit model for the coupled resonator system, with $Z_1(\omega)$ and $Z_2(\omega)$ representing the complex impedance of the DR and DSRR, respectively.

measurements of well characterized ethanol in DI water solutions were made and measured with the sensor. Debye fitting parameters from [39] were used to interpolate the permittivities of ethanol solutions varying from 0 to 100% at exactly the sensor resonant frequency. Solutions of these concentrations were then made up using variable mechanical pipettes and measured with the sensor. In order to fit measurements taken with the coupled DR-DSRR on liquids with known complex permittivity, $\varepsilon^* = \varepsilon' + j\varepsilon''$, resonant parameters of the DR are experimentally obtained (ω_1 and Q_1) via S parameter measurements of the DR without the DSRR or microfluidic channel. Resonant parameters of the empty DSRR are obtained via CST MICROWAVE STUDIO® simulations ($\omega_{DSRR,0}$ and Q_m) and used to calculate the "loaded" DSRR parameters (ω_2 and Q_2) using the interpolated permittivities of the ethanol solutions. The remaining input parameters (k, the inter-resonator coupling coefficient and κ_0, the geometric filling factor) are used as fitting parameters, varied iteratively via a 2-parameter least-squares fit to experimental measurements of ethanol in DI water solutions of different concentrations. The results of the fit to experimental data can be seen in Fig. 7 (a) and (b), showing a good agreement between the experimental results and the mathematical model using the two fitting parameters.

B. Sensitivity analysis

Analysis of the coupled system using the ECM shows that the sensor operates as a transducer, relaying shifts in the resonant frequency of the DSRR via changes in the quality factor, and to a lesser extent the frequency, of the DR resonance. This means that there is no loss in sensitivity from carrying out indirect measurements of the coupled resonator system compared to direct measurement of the frequency shift of the split ring resonator alone, yet high quality factors are maintained, which increases the precision of measurements. This can be seen by using the ECM to calculate comparable, normalized figures of merit (FOM) for

the shifts induced in both the coupled system and the DSRR alone by a theoretical 1% change in permittivity of the material in the gaps away from that of water. As before, permittivity data for water at the sensor resonant frequency is interpolated from [39]. For the coupled system the inverse quality factor shift of the DR, normalized to the full width at half maximum (HW) of the unperturbed system (water condition) can be compared to the frequency shift, again normalized to the full width at half maximum of the unperturbed system, of the DSRR alone:

$$\text{Coupled system FOM} = \frac{\Delta HW_{DR}}{HW_{DR,water}} = \quad (6)$$

$$Q_{DR,water}\left(\Delta\frac{1}{Q_{DR}}\right) = 0.01127$$

$$\text{DSRR alone FOM} = \frac{\Delta f_{DSRR}}{HW_{DSRR,water}} =$$

$$Q_{DSRR,water}\frac{(\Delta f_{DSRR})}{f_{DSRR,water}} = 0.01132 \quad (7)$$

Additionally, the ECM analysis suggests that a $Q_{DSRR,water}$ of less than 3 can be expected for the split ring resonator alone, making measurements more difficult and less precise. The coupled resonator system, therefore, represents a distinct advantage over existing split ring systems, as well as a significant improvement on the sensitivity of resonator based approaches, which have not proved capable of sensing single cells.

C. Background removal

In order to assess the validity of background removal methods, experiments were done to determine the variation of blank measurements without the influence of changing pressure, events at the other capacitive gap, human-caused mechanical wobbles or events at the outlet. This was done by leaving the system to continuously measure the amplitude and phase over more than two hours whilst pumping the background solution through at a constant low pressure (5 mbar). This background data was then treated with a polynomial background subtraction to remove the slow moving drift effects. Amplitude data from these experiments is shown in Fig. 8 (a), along with the same data after polynomial subtraction in Fig 8(b).

Due to sudden mechanical movements such as accidental knocks to the table or cables of the VNA, or doors slamming, bubbles in the channel moving, bubbles at the output bursting or the pooled liquid moving, many experimental data had sudden discontinuities, as well as longer term drift, as shown in Fig. 8 (c).
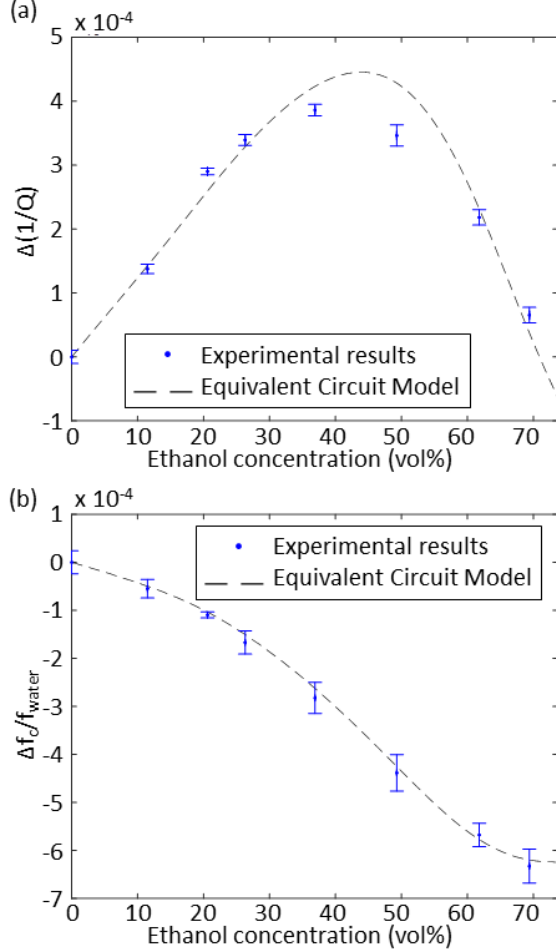
Fig. 7. Plots of experimental data from measurements of ethanol in DI water solutions of varying concentrations (blue points) and the equivalent circuit model (dashed line) evaluated for the associated range of possible solution permittivities corresponding to ethanol concentrations between 0 and 75%, showing the shifts in reciprocal quality factor (a) and in normalized resonance frequency (b). Total length of all error bars denotes two standard deviations of the data. Errors in ethanol concentration small, and are calculated according to pipette accuracy and precision, volume measured and number of separate measurements made for each concentration. For all data points ethanol concentrations and the associated complex permittivity used in the fit are taken from [39].

In order to achieve processing consistency across all datasets, a spline fit to the mean background data in between cell passes was trialed, and the resulting standard deviation of the background data, presented as a histogram in Fig. 8 (f), was compared to the standard deviation of the blank measurements in Fig. 8 (b), shown as a histogram in Fig. 8 (e). Background removal *via* spline fitting was shown to result in a more similar standard deviation of background measurements than the 3rd order polynomial fitting (shown in Fig. 9 (c)). For all results, background removal was therefore done *via* fitting the mean of background measurements with a smoothing spline.
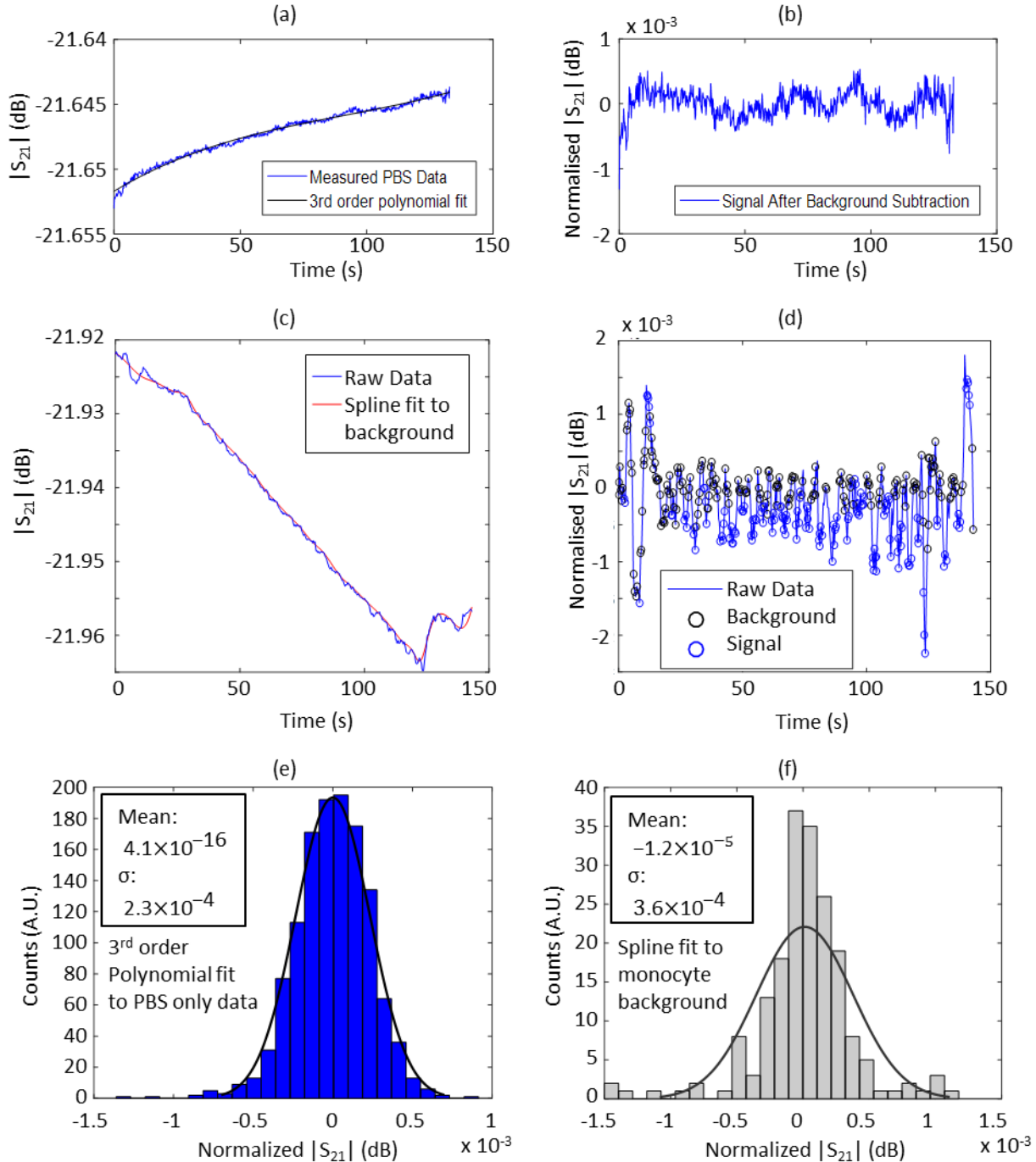

Fig. 8. Plot (a) shows a representative example of the measured $|S_{21}|$ of the coupled resonator sensor with PBS only in the channel, while (b) shows the same data after subtraction of a fitted third order polynomial to remove the effect of long term drift. Plots (c) and (d) show the measured $|S_{21}|$ over several passes of a monocyte cell. In plot (c) the raw data is shown in blue, while a cubic spline fit applied to the background data points is shown in red. Plot (d) shows the same data as in (c) after subtraction of the fit from all data points in order to remove the effect of long term drift and normalize the data around zero. Plots (e) and (f) are histograms of normalized data from measurements. PBS only measurements fitted with a third order polynomial (as plotted in (b)) are shown in (e), while (f) shows the background data from (d) plotted as a histogram.
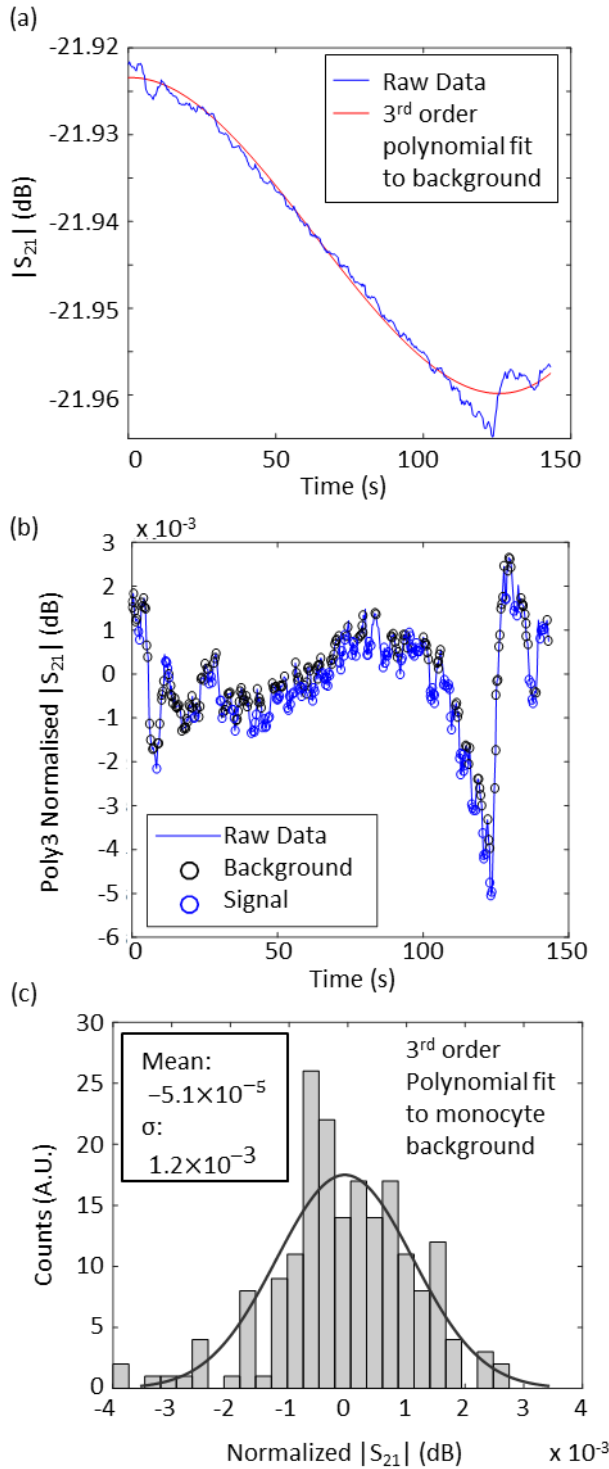
Fig. 9. Alternative background removal applied to the same data as in Fig. 8 (c) for comparison. In plot (a) the raw data is shown in blue, while a third order polynomial fit applied to the background data points is shown in red. Plot (b) shows the same data as in (a) after subtraction of the fit from all data points in order to remove the effect of long term drift and normalize the data around 0, while (c) shows background data from (b) plotted as a histogram.

REFERENCES

[1] H. Fricke and S. Morse, "The electric capacity of tumors of the breast," *J. Cancer Res.*, pp. 340–376, 1926.

[2] P. Mehta, K. Chand, D. Narayanswamy, D. G. Beetner, R. Zoughi, and W. V. Stoecker, "Microwave reflectometry as a novel diagnostic tool for detection of skin cancers," *IEEE Trans. Instrum. Meas.*, vol. 55, no. 4, pp. 1309–1316, 2006.

[3] F. S. Barnes and B. Greenebaum, *Biological and Medical Aspects of Electromagnetic Fields*. 2006.

[4] H. P. Schwan, "Electrical properties of tissues and cell suspensions: mechanisms and models," *Proc. 16th Annu. Int. Conf. IEEE Eng. Med. Biol. Soc.*, pp. A70–A71, 1994.

[5] H. Schwan, "Alternating current spectroscopy of biological substances," *Proc. IRE*, vol. 47, no. 1, pp. 1841–1855, 1959.

[6] H. Schwan, "Analysis of dielectric data: Experience gained with biological materials," *Electr. Insul. IEEE Trans.*, vol. EI-20, no. 6, pp. 913–922, 1985.

[7] A. Surowiec, S. S. Stuchly, and C. Izaguirre, "Dielectric properties of human B and T lymphocytes at frequencies from 20 kHz to 100 MHz.," *Phys. Med. Biol.*, vol. 31, no. 1, pp. 43–53, Jan. 1986.

[8] I. Ermolina, Y. Polevaya, Y. Feldman, B.-Z. Ginzburg, and M. Schlesinger, "Study of normal and malignant white blood cells by time domain dielectric spectroscopy," *IEEE Trans. Dielectr. Electr. Insul.*, vol. 8, no. 2, pp. 253–261, Apr. 2001.

[9] W. Coulter, "High speed automatic blood cell counter and cell size analyzer," *Proc Natl Electron Conf*, vol. 1957, no. 12, pp. 1034–1042, 1956.

[10] V. Gupta *et al.*, "ApoStream™, a new dielectrophoretic device for antibody independent isolation and recovery of viable cancer cells from blood," *Biomicrofluidics*, vol. 6, no. 2, pp. 1–14, 2012.

[11] "ApoCell©." [Online]. Available: http://www.apocell.com/ctc-technology-2/apostreamtm-technology/.

[12] G. I. McIntyre, "Cell hydration as the primary factor in carcinogenesis: A unifying concept.," *Med. Hypotheses*, vol. 66, no. 3, pp. 518–26, Jan. 2006.

[13] H. J. Halpern *et al.*, "Diminished Aqueous Microviscosity of Tumors in Murine Models Measured with in Vivo Radiofrequency Electron Paramagnetic Resonance Diminished Aqueous Microviscosity of Tumors in Murine Models Measured with in Vivo Radiofrequency Electron Paramagnetic Reson," *Cancer Res.*, vol. 59, no. 22, pp. 5836–5841, 1999.

[14] Y. F. Chen, H. W. Wu, Y. H. Hong, and H. Y. Lee, "40 GHz RF biosensor based on microwave coplanar waveguide transmission line for cancer cells (HepG2) dielectric characterization," *Biosens. Bioelectron.*, vol. 61, pp. 417–421, 2014.

[15] K. Grenier, D. Dubuc, M. Poupot, and J. Fournié, "Microwave signatures of alive B-lymphoma cells suspensions," *IEEE*, pp. 95–98, 2011.

[16] K. Grenier, F. Artis, M. Poupot, J. J. Foumié, and D. Dubuc, "Label-free discrimination of human lymphoma cell sub-populations with microwave dielectric spectroscopy," *IEEE MTT-S Int. Microw. Symp. Dig.*, vol. 2018-June, pp. 907–910, 2018.

[17] H. Li *et al.*, "Differentiation of live and heat-killed E. coli by microwave impedance spectroscopy," *Sensors Actuators, B Chem.*, vol. 255, pp. 1614–1622, 2018.

[18] A. A. Abduljabar, X. Yang, D. A. Barrow, and A. Porch, "Modelling and Measurements of the Microwave Dielectric Properties of Microspheres," *IEEE Trans. Microw. Theory Tech.*, vol. 63, no. 12, pp. 4492–4500, 2015.

[19] Y. Yang *et al.*, "Distinguishing the viability of a single yeast cell with an ultra-sensitive radio frequency sensor.," *Lab Chip*, vol. 10, no. 5, pp. 553–5, Mar. 2010.

[20] K. Grenier *et al.*, "Low volume and label-free molecules characterization and cell monitoring with microwave dielectric spectroscopy," *IMBioc 2018 - 2018 IEEE/MTT-S Int. Microw. Biomed. Conf.*, pp. 82–84, 2018.

[21] K. Grenier, D. Dubuc, and T. Chen, "Recent advances in microwave-based dielectric spectroscopy at the cellular level for cancer investigations," *IEEE Trans. Microw. Theory Tech.*, vol. 61, no. 5, pp. 2023–2030, 2013.

[22] C. Dalmay, M. Cheray, a. Pothier, F. Lalloué, M. O. Jauberteau, and P. Blondy, "Ultra sensitive biosensor based on impedance spectroscopy at microwave frequencies for cell scale analysis," *Sensors Actuators A Phys.*, vol. 162, no. 2, pp. 189–197, Aug. 2010.

[23] C. Dalmay, A. Pothier, P. Blondy, F. Lalloue, and M.-O. Jauberteau, "Label free biosensors for human cell characterization using radio and microwave frequencies," *2008 IEEE MTT-S Int. Microw. Symp. Dig.*, pp. 911–914, Jun. 2008.

[24] L. Zhang *et al.*, "Microwave biosensors for identifying cancer cell aggressiveness grade," *IEEE*, pp. 12–14, 2012.

[25] L. Y. Zhang *et al.*, "Discrimination of colorectal cancer cell lines using microwave biosensors," *Sensors Actuators, A Phys.*, vol. 216, no. September 2016, pp. 405–416, 2014.

[26] Z. Ma *et al.*, "Terahertz particle-in-liquid sensing with spoof surface plasmon polariton waveguides Terahertz particle-in-liquid sensing with spoof surface plasmon polariton waveguides," vol. 116102, 2017.

[27] S. M. Hanham, C. Watts, W. J. Otter, S. Lucyszyn, and N. Klein, "Dielectric measurements of nanoliter liquids with a photonic crystal resonator at terahertz frequencies," *Appl. Phys. Lett.*, vol. 107, no. 3, p. 032903, 2015.

[28] O. N. Shaforost, "Microwave whispering-gallery resonators for nanolitre liquid sensing," , PhD thesis University of Dortmund, Germany, 2009.

[29] E. N. Shaforost, N. Klein, S. a. Vitusevich, a. Offenhäusser, and a. a. Barannik, "Nanoliter liquid characterization by open whispering-gallery mode dielectric resonators at millimeter wave frequencies," *J. Appl. Phys.*, vol. 104, no. 7, p. 074111, 2008.

[30] T. Basey-Fisher *et al.*, "Microwaving Blood as a Non Destructive Technique for Haemoglobin Measurements on Microlitre Samples," *Adv. Healthc. Mater.*, pp. 1–7, 2013.

[31] M. Nikolic-Jaric *et al.*, "Microwave frequency sensor for detection of biological cells in microfluidic channels," *Biomicrofluidics*, vol. 3, no. 3, pp. 1–15, 2009.

[32] C. Dalmay, J. Leroy, A. Pothier, and P. Blondy, "Development of high frequency microfluidic biosensors for intracellular analysis," in *Procedia Engineering*, 2014, vol. 87, no. i, pp. 54–57.

[33] N. Meyne, C. Cammin, and A. F. Jacob, "Accuracy enhancement of a split-ring resonator liquid sensor using dielectric resonator coupling," *2014 20th Int. Conf. Microwaves, Radar Wirel. Commun. MIKON 2014*, no. 1, 2014.

[34] R. Narang *et al.*, "Sensitive, Real-time and Non-Intrusive Detection of Concentration and Growth of Pathogenic Bacteria using Microfluidic-Microwave Ring Resonator Biosensor," *Sci. Rep.*, vol. 8, no. 1, pp. 1–10, 2018.

[35] J. C. Chien, A. Ameri, E. C. Yeh, A. N. Killilea, M. Anwar, and A. M. Niknejad, "A high-throughput flow cytometry-on-a-CMOS platform for single-cell dielectric spectroscopy at microwave frequencies," *Lab Chip*, vol. 18, no. 14, pp. 2065–2076, 2018.

[36] Z. Wang *et al.*, "Time domain detection and differentiation of single particles and cells with a radio frequency interferometer," *BioWireleSS 2016 - Proceedings, 2016 IEEE Top. Conf. Biomed. Wirel. Technol. Networks, Sens. Syst.*, no. c, pp. 77–80, 2016.

[37] Y. Cui, W. F. Delaney, T. Darroudi, and P. Wang, "Microwave measurement of giant unilamellar vesicles in aqueous solution," *Sci. Rep.*, vol. 8, no. 1, pp. 1–8, 2018.

[38] D. M. Pozar, *Microwave Engineering*, 4th ed. New York: Wiley, 2012.

[39] T. Sato and R. Buchner, "Dielectric Relaxation Processes in Ethanol/Water Mixtures," *J. Phys. Chem. A*, vol. 108, no. 23, pp. 5007–5015, 2004.

Clare Watts received an MChem degree from the University of Edinburgh, UK in 2013 and a Ph.D. degree from Imperial College London, UK in 2018 on the subject of electromagnetic sensing of single cells. From 2018 to 2019 she was a postdoctoral research associate at Imperial College London working on electronic sensors for cells and biological markers based on surface charge and mass effects.

Stephen M. Hanham (S'03–M'10) received the B.E. and B.Sc. degrees from the University of Western Australia, Australia in 2004 and the Ph.D. degree from the University of Sydney, Australia in 2010. From 2008 to 2010 he was a research project officer and systems engineer at the Commonwealth Scientific and Industrial Research Organization (CSIRO) in Sydney, Australia working on THz antennas and detectors, mobile satellite terminals and radio telescope antenna systems. From 2010 to 2017 he was a postdoctoral research associate and later experienced researcher at Imperial College London, UK. Currently, he is a Senior Fellow and Lecturer at the University of Birmingham, UK. His research interests include electromagnetics, plasmonics, nano-materials, antennas and terahertz and microwave technologies.

James P. K. Armstrong received a PhD in Functional Nanomaterials from the University of Bristol in 2015, and later that year was awarded an Arthritis Research UK Foundation Fellowship to work with Professor Molly Stevens at Imperial College London. He is now an MRC UKRI Innovation Rutherford Fund Fellow in the Department of Materials at Imperial College London, carrying out research that is focused on the development of biotechnologies for tissue engineering and regenerative medicine.

Munir M. Ahmad has a PhD degree in chemistry on the synthesis, electrical and magnetic properties of organic semiconductors. He has worked on the design, synthesis and application of electroactive and specialty polymers. He joined the Optical & Semiconductor Devices Group, Department of Electrical and Electronic Engineering, Imperial College London in 1993 and has worked on a number of projects related to micro-engineering, MEMS and materials for optical devices. He is a Chartered Chemist and a Fellow of the Royal Society of Chemistry.

Molly M. Stevens is Professor of Biomedical Materials and Regenerative Medicine at Imperial College London and Research Director for Biomedical Material Sciences in the Institute of Biomedical Engineering. Her research focuses on materials based approaches to regenerative medicine and biosensing. She is a Fellow of seven academies, including the Royal Academy of Engineering and the Royal Society of Chemistry where she is President of the Division of Materials Chemistry. She has received over 30 major awards, including the 2019 RSC Surfaces and Interfaces Awards and 2016 Clemson Award for Basic Research from the Society for Biomaterials

Norbert Klein is full professor and chair in Electromagnetic Materials at Imperial College London and director of Imperial's Centre of Terahertz Science and Engineering. Before 2009, Prof. Klein was division leader for Electromagnetic Sensors at Juelich Research Center in Germany and was lecturing at Technical Universities of Aachen and Dortmund in Germany. He is (co)author on more than 200 peer-reviewed scientific papers and book articles, and is a key inventor on more than 10 European and US patents related to microwave devices for sensor and communication applications. In 2007 Prof. Klein founded a spin-off company which has successfully commercialized a microwave sensor system for airport security. His current research activities comprise microwave and terahertz sensors for biomedical and security applications and low-dimensional nanomaterials for high frequency applications.